Theoretical and Applied Fracture Mechanics 106 (2020) 102497

Contents lists available at ScienceDirect

Theoretical and Applied Fracture Mechanics

journal homepage: www.elsevier.com/locate/tafmec

Mode I and II fracture toughness investigation of Laser-Sintered Polyamide

Emanoil Linul, Liviu Marsavina, Dan Ioan Stoia*

Department of Mechanics and Strength of Materials, Politehnica University of Timisoara, 1 Mihai Viteazu Avenue, 300 222 Timisoara, Romania

ARTICLE INFO

Keywords:
Four-point bending tests
Mode I and II fracture toughness
Lased-sintered polyamide
Process energy and spatial orientation

ABSTRACT

This paper presents experimental investigations on the geometrical and fracture properties of specimens obtained by Additive Manufacturing technology. The experimental tests were performed on Single Edge Notch Bend (SENB) specimens obtained through the Selective Laser Sintering process, based on the polyamide PA2200 material. The SENB specimens were manufactured using three different process energies-PEs (E1, E2 and E3), respectively three different spatial orientations-SOs (Vertical-V, Horizontal-H and Oblique-O). Symmetric and asymmetric four-point bending tests were used to determine the mode I and II fracture toughness (K_{IC} and K_{IIC}). It was observed that the density (ρ) of the 3D printed specimens is highly dependent on the PE and SO, the highest density values being obtained for the highest PE (E1), respectively for the V-SO. Maximum relative errors of the main geometrical parameters (thickness, length and width) of the SENB specimens were obtained for E3-PE and H-SO. With respect to the fracture toughness, it was observed that, regardless of PE and SO, the K_{IC} values are higher than K_{IIC} ones. The highest K_{IC} value was found for E1 and V-SO, while K_{IIC} highlight the highest value for E1 and H-SO. Finally, analysis of variance (ANOVA) method is used to analyze the influence of various factors on outcome parameters.

1. Introduction

One of the most outstanding features of additive manufacturing (AM) technology is the geometrical versatility of the parts that can be produced, at relatively low manufacturing costs [1–3]. The properties of the parts are close related to process parameters and due to the lack of standardization, the mechanical characterization is required for every technology [4–6].

There are many efforts in characterization of AM parts. The strain rate influence of the additive manufactured PA12 on the failure load was studied for tensile specimens [7]. The low rate tensile test was conducted in accordance with [8], while the high rate tests were conducted using Hopkinson pressure bar, also in tension. Higher failure loads were recorded for higher strain rates. The stress-strain curves obtained for low tension rate exhibit non-linear behavior and provides similar mechanical properties to those of PA12 conventionally manufactured. Some other authors studied the influence of the surface aspect of AM parts as an important issue that directly derives from the process. The effect of surface roughness on the fatigue performances of titanium alloyed specimens was studied, underlining the crack initiation in relation to surface integrity [9]. Specimens obtained by fused filament fabrication having different orientations were tested in order to determine the fracture behavior in layered materials [10]. Also, they conduct numerical simulations using XFEM, and compare the results afterwards. Brittle, ductile and kinked fracture behavior were associated with filament orientation during manufacturing process. Tensile testing was extensively conducted on PA 12 (PA2200) [11–13]. The effect on elongation to break and mechanical strength according to the sinterization process was studied by Craft et al. [14]. Significant differences were underlined according to the manufacturing process. The influence of loading configuration on the fracture toughness was determined by Poapongsakorn and Carlsson [15], on PVC foams using single edge-notched beam specimens in three and four-point bending. The results are showing significantly higher fracture toughness obtained in four-point bending test. Also, the linear relation between the specimen density and K_{IC} is revealed.

Crack growing in tensile test, according to building directions was studied by Riemer et al. [16], for titanium specimens produced by selective laser melting. They proved that substantial improvement of crack resistance behavior can only be achieved by heat treatment. Extensive studies on full range loading conditions including pure delamination modes and mixed modes I/II, I/III and II/III were successfully conducted on different composite structures and porous materials [17–20]. It was found that, in-plane and out-of-plane loading angle, density, testing conditions plays a decisive role on fracture toughness [21–24]. The asymmetric four-point bending tests has received special

* Corresponding author.
E-mail address: dan.stoia@upt.ro (D.I. Stoia).

https://doi.org/10.1016/j.tafmec.2020.102497
Received 23 December 2019; Received in revised form 16 January 2020; Accepted 16 January 2020
Available online 17 January 2020

Nomenclature

a	crack length
B	thickness of the specimen
d	scan spacing
E	energy density
F_{max}	maximum force
$f_I(a/W)$	mode I stress intensity factor
$f_{II}(a/W)$	mode II stress intensity factor
h	beam offset
H, V, O	horizontal, vertical and oblique orientation
I_K	fracture toughness index
K_{IC}	mode I fracture toughness
K_{IIC}	mode II fracture toughness
L	length of the specimen
P	laser beam power
PE	process energy
P_Q	critical fracture load
Q	shear force
SENB	single edge notch bending specimen
SF	scaling factors
SO	spatial orientation
t	layer thickness
T_1	building chamber temperature
T_2	removal chamber temperature
v	velocity of laser beam
W	width of the specimen
Err L, Err B, Err W	relative error of length, thickness and width
4 PB	four-point bending test
σ	normal stress
ρ	density
τ_0	shear stress

attention over the years [25–27]. Due to the relatively simple loading configuration, different teams of researchers determined the fracture behavior of concrete [28–31], granite [32–34], foams [35], pure titanium [36] and extruded polystyrene [37] materials. Moreover, the theoretical prediction of the experimental results was intensively studied by Mirsayar and co-workers [38,39], Torabi and co-workers [40,41], and Aliha and co-workers [42,43], using different theories and fracture criteria. In addition, fracture properties determined using a significant number of AM specimens were determined by Ahmed and Susmel [44] on PLA and by Razavi and Berto [45] and Solberg et al. [46] on metallic materials produced by laser melting.

To the best knowledge of the authors, there are no results reported in the literature related to mode I and mode II fracture toughness of laser-sintered Polyamide, under four-point bending (4 PB) tests. Therefore, for investigating the main fracture properties, this paper uses single edge notch bend specimens in symmetric and asymmetric 4 PB testing fixtures. Also, the influence of three different process energies and spatial orientations have been investigated. In addition, the influence of various factors on outcome parameters was analyzed using analysis of variance (ANOVA) method.

2. Materials and methods

2.1. Materials

This investigation is based on the polyamide PA2200 material used for specimens manufacturing, which is an EOS (Electro Optical Systems - EOS GmbH, Germany) commercial product. In its powder form, PA2200 is suitable for sinterization, the resulted parts exhibiting good physical and mechanical properties, despite the porous structure. The internal structure of PA2200 is directly influenced by the following main factors: process energy, layer thickness, particle size and powder spreading. Some physical, biological and mechanical properties were determined by the producer: grain size of 56 μm according to ISO 13320-11 [47]; bulk density according to EN ISO 60 is 0.45 g/cm^3 [48]; melting point 172–180 °C according to EN ISO 11357-1 [49]; biocompatibility according to EN ISO 10993-1 [50] and USP/level VI/121 °C; food contact approval in compliance with the EU Plastics Directive 2002/72/EC [51].

2.2. Methods

The study comprises of five stages: specimen CAD design, additive manufacturing process, mass and geometry assessment, mechanical testing and statistical validation of data. In each step specific equipment, methods and software have been used.

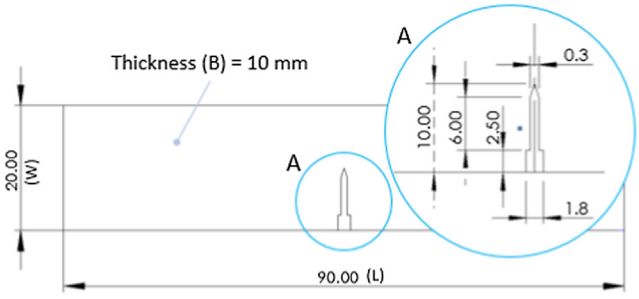

Fig. 1. 3D specimen model.

2.2.1. Specimen design and additive manufacturing

The specimen geometry (Fig. 1) was designed in SolidWorks 2017 according to the specifications of ASTM D 5045-99 standard [52]. The notch was designed on the 3D model of the specimen having a width of 0.3 mm and a total length of 10 mm and was formed during additive manufacturing process. In order to avoid the specimens wrapping and/or twisting during manufacturing process, the notch was closed on the first 2.5 mm from the outer bottom surface. The bridge between the crack flanks was removed mechanically using an electrical saw blade for cutting 2.5 mm in width of the specimen, along the notch direction.

The specimens were positioned in three ways that materialize three spatial orientations (SOs): (i) vertical orientation (V = 90°) having the width dimension (W) of the specimen along with the growing direction (Z direction), (ii) horizontal orientation (H = 0°) having the thickness dimension (B) aligned with the Z growing direction, and (iii) oblique orientation (O = 45°) having the frontal plane of the specimen angular oriented to the horizontal XY plane of the machine (see Fig. 2). Ten specimens were organized for each SO and connection ribs were built in order to prevent geometrical distortions.

The additive process was conducted on EOS Fromiga P100 machine

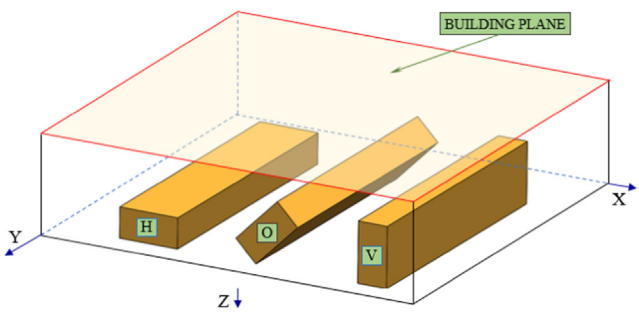

Fig. 2. Positioning of the specimens according to SO.

using three different process energies (PEs): E1, E2 and E3, which are presented in the Table 1. The parameters from Table 1 presents the follows notations: P-laser power; v-scanning velocity; E-energy density, as function of power, velocity and scan spacing; d-scan spacing; h-beam offset; T_1-temperature of the building chamber; T_2-temperature of the removal chamber; t-layer thickness; SF-scaling factors on XY and Z directions. Powder bed is the height of the non-sintered powder placed at the beginning and at the end of the manufacturing process.

By positioning 10 specimens for each spatial orientation and considering 3 process energies, a total number of 90 specimens were manufactured.

Formiga P100 machine uses a 30 W CO_2 laser for layer-by-layer sinterization of plastic powders. It consists of two main chambers: building chamber, were the process occurs and the removal chamber were the parts are lowered and cooled down. The chambers are set up to different temperatures: 170 °C for building and 159 °C for removal through independent electrical heating sources. The heat convection and conduction ensure the softening temperature for the powder in the building chamber, so that the laser gives only the additional energy required for sinterization. The oxygen content of the chambers in controlled by the machine under 0.5%.

The powder is flowing from two barrels placed on the top of the machine, and it is uniformly spread by a mechanical arm using a sweeping blade.

The laser beam has the focal plane on the zero level of the building chamber and a spot diameter of 0.42 mm. The spot size is therefore directly limiting the minimum wall thickness of a part.

The additive process runs for 9 h for each energy. At the end of manufacturing, the parts cool down for another 18–20 h and after that were removed from the machine (Fig. 3) and air blasted.

2.2.2. Mass and geometry assessment

Next step in study was to determine the mass and linear dimensions of each individual specimen, in order to compute the density (ρ) and to verify the relative dimensional error. The measurements were conducted on L, B and W dimensions using a Mitutoyo digital caliper of 0.02 mm accuracy. All measurements were repeated three times in order to obtain average value of every dimensional parameter/specimen.

The specimens were then weighted using a Kern laboratory balance of 0.01 g accuracy. Having the mass and computing the volume for each specimen, the individual densities were obtained.

By visual inspection, it was observed that the obtained laser-sintered specimens had no defects, such as pores, separation of layers or cracks, and no signs of internal stress were detected.

2.2.3. Fracture properties assessment

All experimental tests were carried out using a Zwick Roell standard electromechanical universal testing machine with a maximum load-cell capacity of 5 kN, controlled by a constant crosshead displacement of 5 mm/min for all specimens. For the evaluation of the fracture properties, four-point bending (4 PB) tests and single edge notch bending (SENB) specimens were adopted [53]. The loading configuration of the investigated specimens was designed to obtain both the mode I (K_{IC}) and mode II (K_{IIC}) fracture toughness values.

Details of experimental testing set-up and used procedure are presented in Fig. 4. Assessment of K_{IC} was performed on symmetrically loaded SENB specimens (see Fig. 4a), while for K_{IIC} an asymmetric loading configuration was assumed (see Fig. 4b).

Dimensions and loading configuration of 4 PB test specimens are also shown schematically in Fig. 4. The distance between the supports for the symmetrical fixture was set at $4W$ (≅80 mm), while the loading points at a distance of $2W$ (≅40 mm). In the case of asymmetrically loaded SENB specimens, the distance between the supports and the loading points ($b_1 + b_2$) was considered as equal to five times the width/thickness of the specimen ($5B$), that is about 50 mm (b_1 = 10 mm and b_2 = 40 mm). In both cases (symmetric and asymmetric loading), as mentioned above, the specimen crack (a) kept the same length (a ≅ 10 mm), and the load was applied along it (parallel to the crack flank) [35]. Aliha and co-workers [54,55] showed that for small values of b_1/W ratio, the effect of T-stress on mode II deformation is high. Therefore, in choosing the dimensions of the specimens, it was taken into account that the location of supports and their distance from the crack tip do not significantly affect the crack tip stress field.

The experimental tests under 4PB fixture were performed in accordance with ASTM D 5045-99 standard [52], while the testing temperature was controlled to be within the range 25 ± 2 °C.

2.2.4. Data processing and statistics

In order to validate the data and to determine the significance of the recorded differences, one-way analysis of variance (ANOVA) was used for the outcome parameters: density, length, thickness, width, mode I fracture toughness and mode II fracture toughness, in relation to the PO (E1, E2 and E3) and SO (V, H and O). In addition, the Pearson's correlation was used to determine how strong is the relation between input technological variables and outcome parameters [56].

3. Results and discussions

3.1. Geometric properties

For all 90 specimens, linear measurements were conducted prior to mechanical testing. For each specimen different geometrical parameters (L, B and W) were acquired three times and the average value of these was further taken into consideration. The measured values (m_{val}) were then used together with the nominal dimensions (n_{val}: L = 92.1 mm, B = 10.23 mm and W = 20.46 mm) in order to determine the relative error, in accordance to the Eq. (1).

$$Err[\%] = \left|\frac{m_{val} - n_{val}}{n_{val}}\right| \cdot 100 \quad (1)$$

The density of the specimens is highly dependent on the SO and PE (Fig. 5). The values here presented are averages and as we expect higher energy of sinterization (E1) conduct to higher density due to larger fusion bridges between powder particles. From the orientation point of view, V-SO of the specimen always lead to better density. This may be the influence of the powder spreading in relation to the specimen orientation (sweeping blade generates a local settle down of the powder.), and the number of layers that composes the part (200 layers). The standard deviation of density shows a slight data spread.

Maximum relative errors (%) of geometrical parameters were recorded for specimen thickness in the case of E3-PE and H-SO (about 9.5%). As can be seen in Fig. 6a, less dependent dimensional error in relation to the PE and SO was obtained for the total length of the

Table 1
Laser sintering parameters.

SO [°]	P [W]	v [mm/s]	E [J/mm^2]	No. of layers	d [mm]	h [mm]	T_1 [°C]	T_2 [°C]	t [mm]	SF [%]	Powder bed [mm]
H	25	1500	E1 = 0.067	100	0.25	0.15	170	159	0.1	2.3	60
O	23	2000	E2 = 0.046	212							
V	21	2500	E3 = 0.034	200							

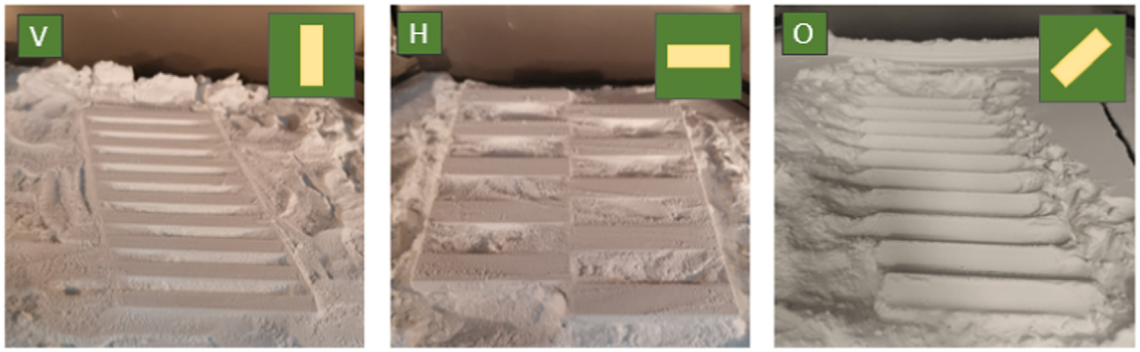

Fig. 3. Images of the specimens before machine removing: V (a), H (b) and O (c) spatial orientations.

specimen (L), meaning that larger dimensions are less influenced by the process parameters [11–13]. The thickness error (Err B) was very similar for the E1 and E2 energies, with low standard deviation and identic trend regarding the SO (see Fig. 6b). The errors determined for E3-PE however are proving a dimensional instability of the SLS process.

The error of specimen's width (Err W) seems to be very low and consistent for all three PEs in the case of V-SO of the specimens (see Fig. 6c). On the other hand, the horizontal positioning (H-SO) lead to high relative errors very dependent on PE.

As a general observation, the growing direction of the specimens (Z direction of machine) determine smaller relative errors, as it can be observed from Fig. 6b and c (orientation O-SO for *Err B* and V-SO for *Err W*). Another conclusion that emerged from the error graphs is that higher PE influences the dimensional stability of the process in a convenient manner.

3.2. Fracture properties

In order to visualize the initiation and propagation of the crack for different process energies (PEs) and spatial orientations (SOs) of the specimens, during the 4PB tests, recordings of all the symmetric and asymmetric tests were made. Fig. 7 illustrates the initial specimens (before bending tests-Fig. 7a, e) and crack propagation paths (after bending tests-Fig. 7c, g) for a specimen from the horizontal (H) plane, obtained with an E_2 energy density.

From the visual inspection of the crack path in SENB specimens, regardless of the loading mode (mode I or II fracture), the crack growth started from the crack tip (see Fig. 7d, h) [57]. The symmetrically loaded specimens show a propagation path along the crack, until the final fracture of the specimen occurs [26]. Taking into consideration that the state stress of the crack section in 4 PB test specimen is pure bending, it is well-founded to conclude that the slight deflection (zigzag waves) of crack propagation path is mostly related to the existence of material layers obtained during 3D printing, and the effect of shear

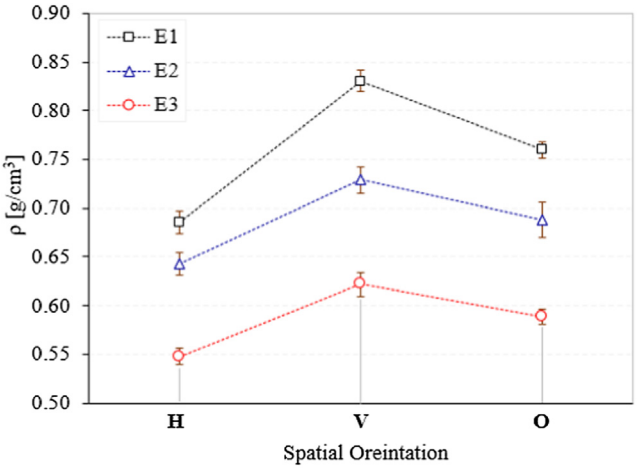

Fig. 5. Specimens density (ρ) according to PE and SO.

force is insignificant (see Fig. 7d). On the other hand, the asymmetric loading exhibit an inclined propagation path (see Fig. 7h), the final fracture of the specimen taking place under the first (left) loading point [58].

During the 4PB tests, applied load P and displacement Δ were automatically recorded and collected using a data acquisition system incorporated into the testing machine [59,60]. Figs. 8 and 9 show the P-Δ curves obtained for symmetrical and asymmetrical loading fixtures. Specifically, Fig. 8 shows the influence of the SO (H, O, V) on the fracture behavior of the SENB specimens for the three investigated PEs (E_1, E_2, E_3). Fig. 9 shows the same behavior, except that it shows the influence of PE for the three investigated SOs. Regardless of the group of curves analyzed, it can be observed that they have a very small area of settlement, followed by a linear-elastic region at the end of which the

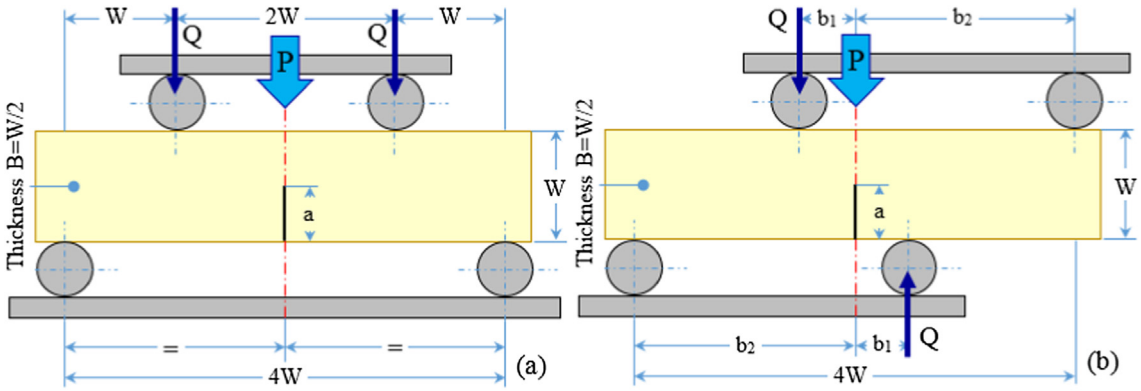

Fig. 4. Experimental set-up for symmetric (a) and asymmetric (b) loading configuration.

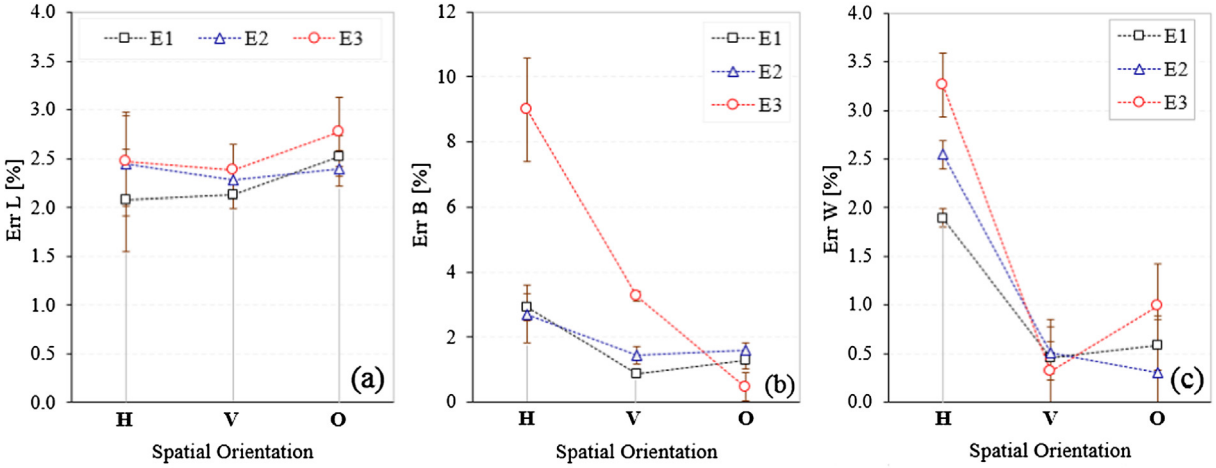

Fig. 6. Relative error of length (a), thickness (b) and width (c) according to PE and SO.

ultimate load capacity (maximum load) is found. Once the peak load was reached, the specimen either breaks suddenly (e.g. Fig. 8b curve for the V-SO) or shows a progressive decrease in load carrying capacity (e.g. Fig. 8b curve for the O-SO), followed by a brittle fracture [61,62]. Notably, the progressive decrease in load have been found for specimens printed in the O-SO direction, while a sudden brittle fracture was obtained for the other two SOs (H-SO and V-SO).

As can be observed from Figs. 8 and 9, the P-Δ curves obtained from specimens in the same group presents major differences, which means that both the PE and the SO significantly influence the fracture behavior of the investigated SENB specimens. From Fig. 8 it can be observed that the SO presents the highest differences in terms of load and displacement, this being observed especially for symmetrical loading (mode I fracture). On the other hand, PE has major differences in terms of both loading configuration (symmetric, asymmetric) and SO.

The analysis of the P-Δ curves represents an important aspect because depending on their interpretation the fracture toughness will be calculated. The mode I (K_{IC}) and mode II (K_{IIC}) fracture toughness were determined according to [63] based on Eqs. (2) and (3):

$$K_{IC} = \sigma\sqrt{\pi a}\cdot f_I\left(\frac{a}{w}\right) \tag{2}$$

$$K_{IIC} = \tau_0\sqrt{\pi a}\cdot f_{II}\left(\frac{a}{w}\right) \tag{3}$$

where a is the crack length in [mm], while σ and τ_0 [MPa] are the normal and shear stresses corresponding to the mode I and II loading, and are calculated with the Eqs. (4) and (5) [63]:

$$\sigma = \frac{3P_Q l}{BW^2} \tag{4}$$

$$\tau_0 = \frac{P_Q - Q}{BW} \tag{5}$$

were l (distance between the first support and the first loading point) = W (specimen height) in [mm], B is specimen thickness (depth) in [mm] and P_Q is the critical fracture load in [N]. Taking into account the suggestions of the ASTM D5045-99 standard [52], the determination of the critical fracture load P_Q from the P-Δ curves was done accordingly.

From Fig. 4b it can be seen that the asymmetric configuration is both in static equilibrium and statically determined. Therefore, in Eq. (5) the shear force, Q, which acts between inner loading points, is related to the force P_Q and is given by Eq. (6) [64]:

$$Q = P_Q\frac{(b_2 - b_1)}{(b_2 + b_1)} \tag{6}$$

Finally, the geometric stress intensity factors $f_I(a/W)$ and $f_{II}(a/W)$, expressed in terms of ratio between crack length and the height of the specimen a/W, are determined for both loading fixtures (symmetric and asymmetric configurations) using the polynomial Eqs. (7) and (8), as follow [63]:

$$f_I\left(\frac{a}{W}\right) = 1.122 - 1.121\frac{a}{W} + 3.740\left(\frac{a}{W}\right)^2 + 3.873\left(\frac{a}{W}\right)^3 - 19.050\left(\frac{a}{W}\right)^4 + 22.550\left(\frac{a}{W}\right)^5 \tag{7}$$

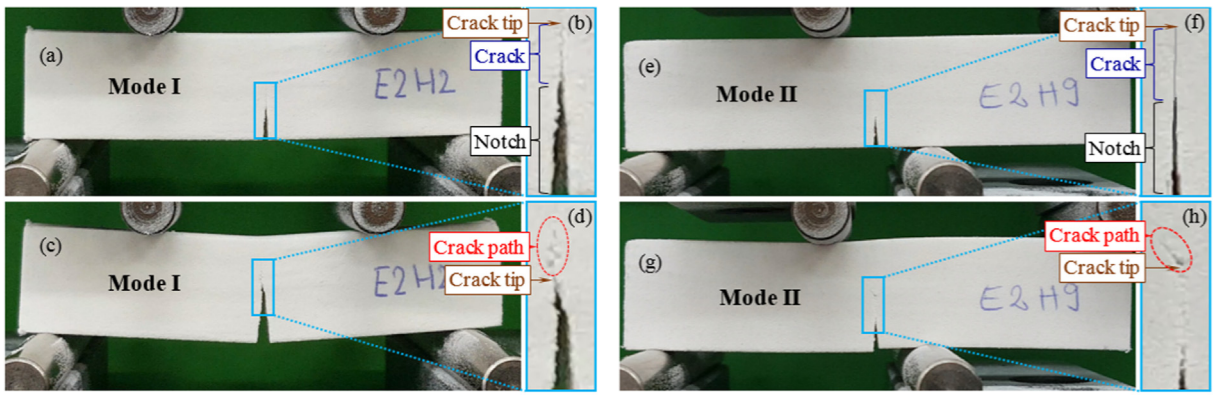

Fig. 7. Initial (a, e) and tested (c, g) 4PB specimens under mode I and II loading.

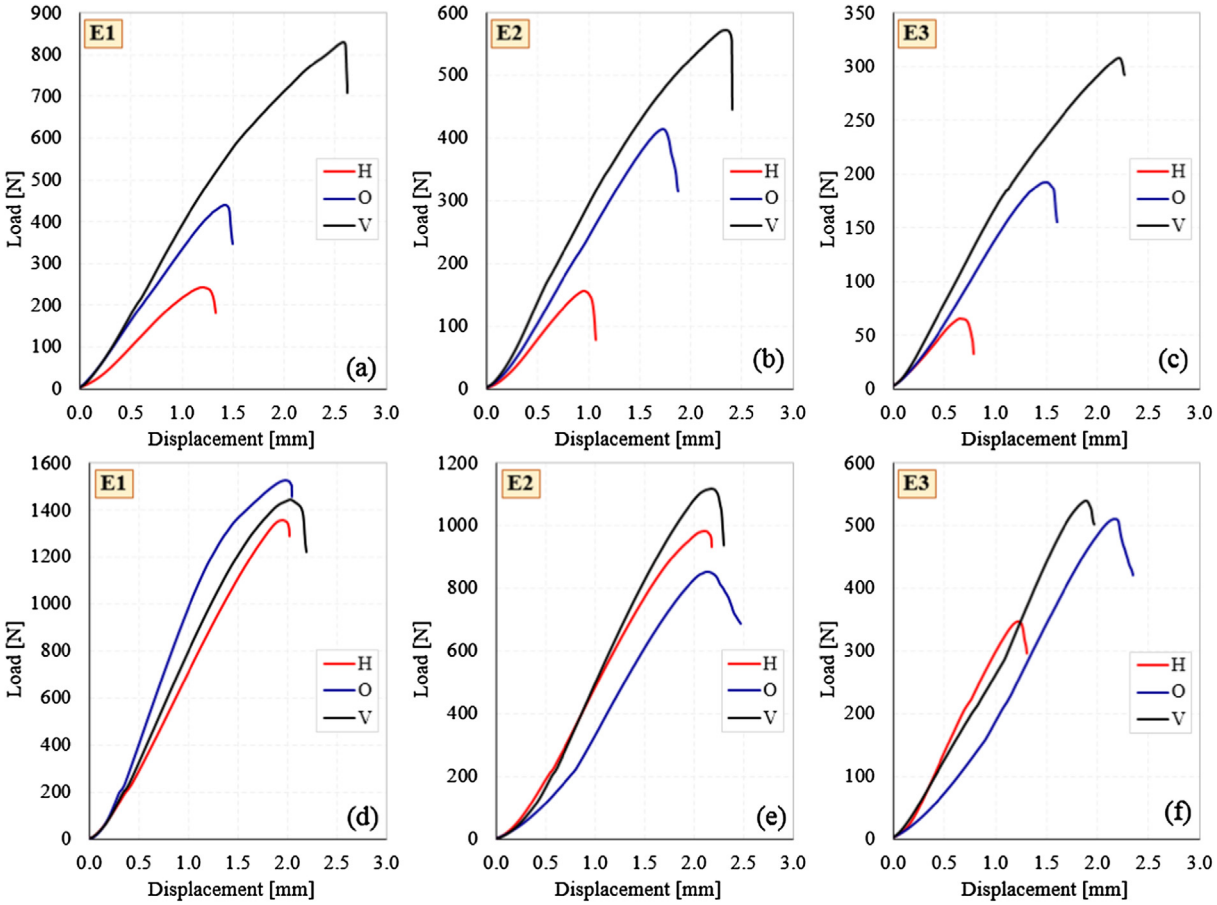

Fig. 8. Load-displacement curves under mode I (a, b, c) and mode II (d, e, f) fracture. Influence of SO.

$$f_{II}\left(\frac{a}{W}\right) = -0.2915 + 6.3229\frac{a}{W} - 9.1199\left(\frac{a}{W}\right)^2 + 6.0570\left(\frac{a}{W}\right)^3 \quad (8)$$

It should be mentioned that for asymmetric four point pending a small amount of Mode I stress intensity factor is present due to the finite geometry of the specimen [63]. However, this value is approximately 18 times smaller than the Mode II value and was neglected in the further calculations.

In order to highlight the dependence of the K_{IC} and K_{IIC} values with the specimen density (ρ), it is necessary to introduce a new parameter, called *fracture toughness index* I_K. Parameter I_K is defined for each loading mode (mode I and II) by the Eq. (9) [65]:

$$I_{K,i} = \frac{K_{iC}}{\rho},\ i = I, II \qquad [\text{MPa}\cdot\text{m}^{3.5}/\text{kg}] \quad (9)$$

Taking into account all the Eqs. (2)–(9), Tables 2 and 3 lists the average values of the obtained results for both symmetric and asymmetric loading configurations. The experimental results are presented for both SO and PE.

Figs. 10 and 11 show the variation of the fracture toughness (K_{IC} and K_{IIC}) with PE, respectively SO. From these figures, it can be observed that both PE and SO have significant influences on K_{IC} and K_{IIC}. Regardless of PE and SO, the K_{IC} values are higher than the K_{IIC} values; this being consistent with the literature reported results on other types of polymeric materials [20,25,66]. From Fig. 10a it is observed that K_{IC} respects the same pattern according to the used PE. The highest K_{IC} values are obtained for V-SO, followed by O-SO and H-SO respectively. The mode I fracture toughness values in the V-SO is higher by up to 51.86% (for E1) compared to the one in the H-SO. This difference increases linearly up to 69.81% (for E3) with the decrease of PE. Mode II fracture toughness presents approximately the same values for H-SO and O-SO (for E1 and E2), while in the V-SO, lower values are obtained with about 15% (Fig. 10b). It was found that the K_{IIC} values for E3 do not follow the same pattern with the other two energies (E1 and E2). This aspect may be associated with the difficult placement of the specimens due to geometrical errors (see Section 3.1). The mode I of fracture did not meet these problems because the loading was done symmetrically.

Analyzing Fig. 11 it can be observed very easily that regardless of the SO, all the K_{IC} and K_{IIC} values decrease significantly with the decrease of PE. However, taking into account the SO, the largest differences in K_{IC} and K_{IIC} values, up to about 79%, are obtained for the H-SO (from E1 to E3). In contrast, the V-SO shows the smallest decreases in K_{IIC} values (up to 40.18%) depending on the PE decrease (see Fig. 11b).

On the other hand, from Tables 2 and 3 (last column) it can be deduced that K_{IC} and K_{IIC} are density-dependent, the density of specimens highlighting a major influence on the fracture toughness values. Considering this density-properties dependence, Fig. 12 shows the variation of fracture toughness (K_{IC} and K_{IIC}) data with the specimen's density (ρ).

It has been observed that regardless of the loading configuration (symmetric or asymmetric), PE (E1, E2 or E3) and SO (H, V or O), the mode I and mode II fracture toughness values increase with increasing of specimen's density. In most cases, with very small exceptions, this increase is linear.

Fig. 12 actually displays some maps of distribution of K_{IC} and K_{IIC} values according to PE and SO. These maps have a particular importance in the optimization processes of the materials used in different engineering applications. Therefore, knowing the type of used material (in this case PA 2200), by visualizing these fracture toughness-density maps, one can predict the values of K_{IC} and K_{IIC} without carrying out 4PB experimental tests. This helps to eliminate the time of production

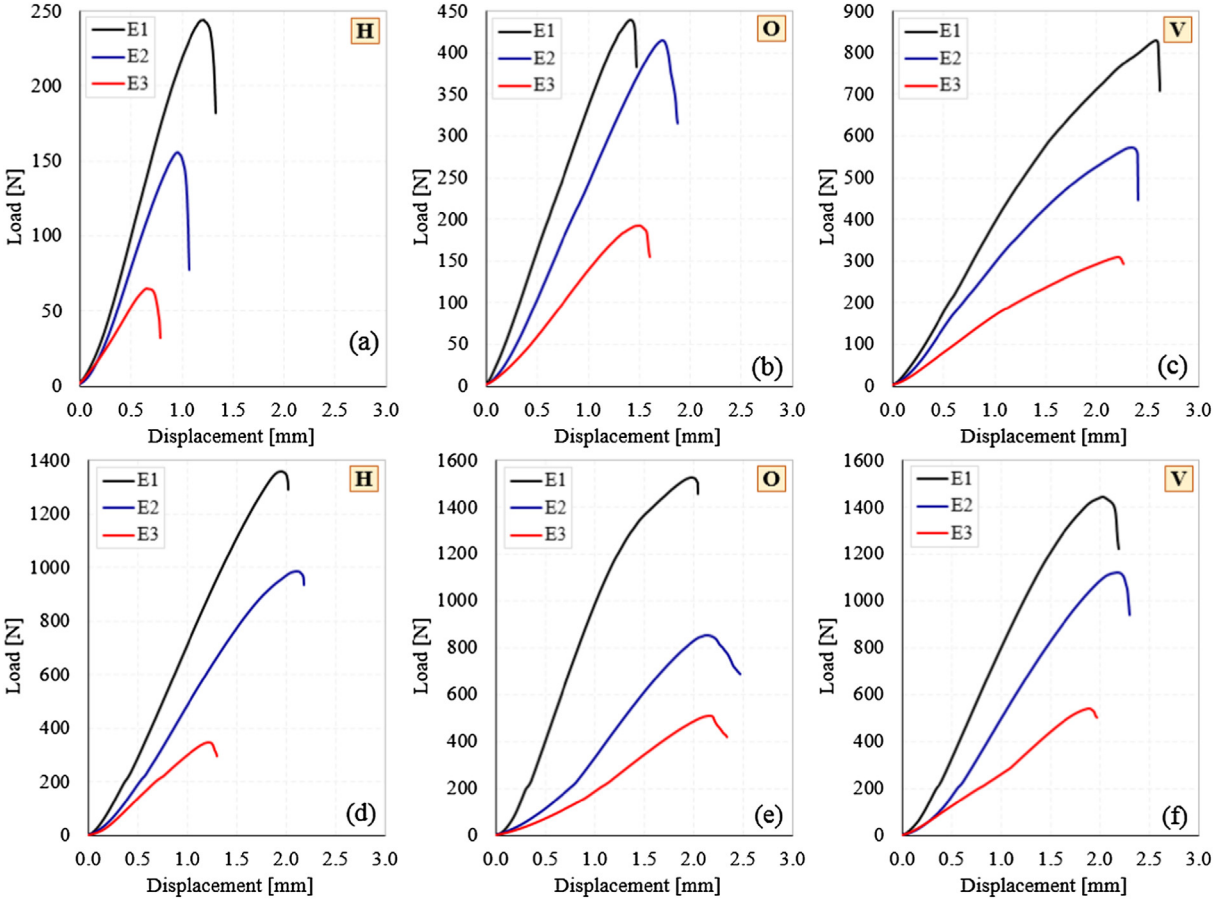

Fig. 9. Load-displacement curves under mode I (a, b, c) and mode II (d, e, f) fracture. Influence of PE.

of the specimens and to carry out the experimental tests, respectively to reduce the costs regarding the production and the testing of the specimens. Ultimately, it is desirable to make such distribution maps of the properties for different engineering materials tested under different loading conditions.

Typical mode I and II fracture paths of broken laser-sintered specimens obtained using E1 process energy are shown in Fig. 13. Based on the experiments, PE does not affect the crack propagation paths, while SO substantially changes the fracture path. The mode I fracture path in H and O directions is stable and grows following a straight line along the notch plane (Fig. 13a, b). For mode II loading, the crack initiation makes an angle to the notch plane, of following values: 54.5° for H-direction of sample grow and 58.4° for the V-direction (Fig. 13d, e). Finally, the propagated crack stops under the nearest loading point, completing the test.

The samples having vertical direction of growing possesses a notch direction perpendicular to the layer deposition and bonding. In this case, both loading modes I and II lead to lower fracture strength of the layer interface than the layer itself. Therefore, the crack direction has a preference growth (shear effect) along the layer bonding interface. This debonding is followed by the crack growth, which for mode I tends to propagate in the plane of the crack (Fig. 13c), while for mode II the path ends under the loading point (Fig. 13f). The samples growth in the horizontal and oblique position have a notch direction parallel and respectively oblique to the layer deposition and bonding, and therefore no debonding effect is recorded.

Based on Fig. 13, all the SENB specimens made of Laser-Sintered Polyamide were fractured from the crack tip without any local damage from supports or loading points.

3.3. Data statistics

Quasi-static Pearson's correlations (see Table 4) evidence a linear relation between the additive parameters: process energy *PE* and spatial

Table 2
Mean values of mode I fracture properties according to PE and SO.

Process energy	Spatial orientation	ρ [g/cm^3]	F_{max} [N]	P_Q [N]	Q [N]	σ [MPa]	K_{IC} [MPa·m$^{0.5}$]	$I_{K,I}$ [MPa·m$^{3.5}$/kg]
E_1	H	0.684	304.318	288.880	144.440	4.152	1.098	1604.731
	V	0.832	877.860	591.660	295.830	8.566	2.282	2739.072
	O	0.758	407.097	361.617	180.808	5.264	1.403	1849.691
E_2	H	0.638	189.887	174.368	87.184	2.520	0.664	1040.214
	V	0.720	524.018	424.272	212.136	6.180	1.647	2283.027
	O	0.687	372.790	334.813	167.407	4.891	1.302	1889.890
E_3	H	0.551	68.038	62.518	31.259	0.885	0.232	419.774
	V	0.629	291.428	195.540	97.770	2.874	0.767	1220.410
	O	0.599	165.778	158.903	79.451	2.227	0.598	731.689

Table 3
Mean values of mode II fracture properties according to PE and SO.

Process energy	Spatial orientation	ρ [g/cm^3]	F_{max} [N]	P_Q [N]	Q [N]	τ_0 [MPa]	K_{IIC} [MPa·m$^{0.5}$]	$I_{K,II}$ [MPa·m$^{3.5}$/kg]
E_1	H	0.687	1313.158	1233.704	740.222	3.506	0.836	1214.309
	V	0.833	1505.910	986.144	591.686	2.877	0.692	829.224
	O	0.764	1365.510	1151.600	690.960	3.391	0.813	1062.531
E_2	H	0.642	990.290	881.455	528.873	2.553	0.606	943.848
	V	0.738	1195.326	637.302	382.381	1.876	0.450	609.181
	O	0.675	958.624	848.242	508.945	2.483	0.598	884.770
E_3	H	0.544	326.320	283.678	170.207	0.766	0.181	332.350
	V	0.610	577.533	577.533	346.520	1.714	0.414	677.977
	O	0.587	584.875	537.660	322.596	1.547	0.374	637.414

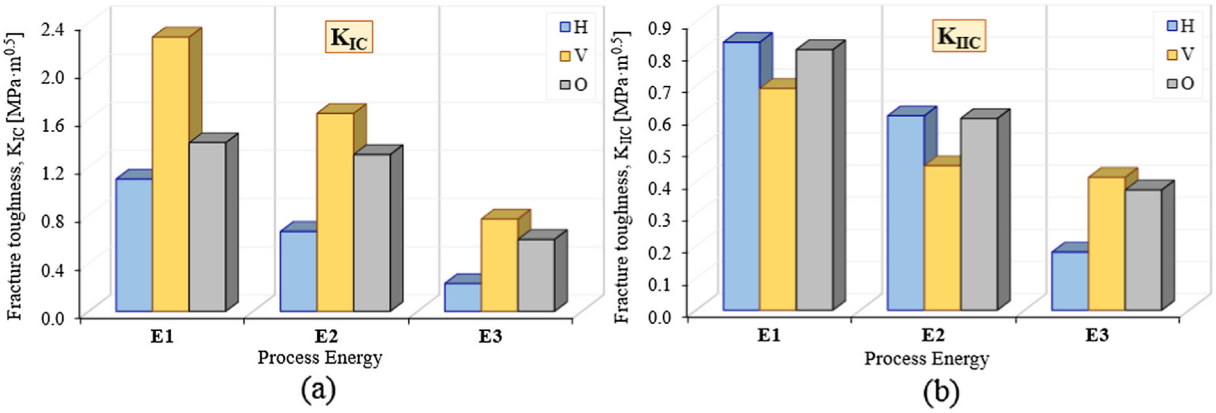

Fig. 10. Mode I (a) and mode II (b) fracture toughness variation according to PE. Influence of SO.

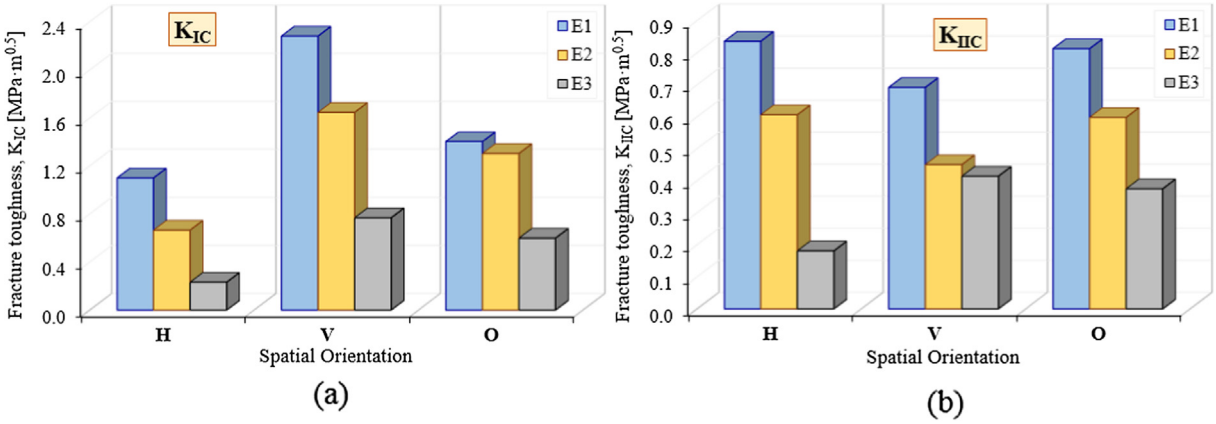

Fig. 11. Mode I (a) and mode II (b) fracture toughness variation according to SO. Influence of PE.

orientation *SO* and the outcome variables: density ρ, length *L*, thickness *B*, width *W*, mode I fracture toughness K_{IC} and mode II fracture toughness K_{IIC}. Strong positive correlation of density with both additive parameters (PE and SO) can be observed. The length *L* of the specimens shows very little connection with the SO for E1, while the thickness *B* shows a strong negative correlation with the SO, for all three PEs (E1, E2 and E3). The K_{IC} confirm a strong positive correlation with both PE and SO, while K_{IIC} has positive correlation only for the PE and negative correlation for SO.

In order to demonstrate the statistical signification of the outcome variables, the one-way ANOVA was used for density and fracture toughness determined for all SOs (H, V, O) and all PEs (E1, E2, E3). The ANOVA parameters presented are: Source of Variation – Between groups (BG) and Within Groups (WG); Sum of squares (SS); Degrees of freedom (df); F value (F); P value (p) and F critic (F crit.) [67].

According to Table 5, statistically significant differences between the specimens densities obtained at E1, E2 and E3 were determined for each spatial orientation ($p \ll 0.05$). The highest significant difference of energy-density relation is recorded for vertical spatial orientation (V-SO) of the specimens ($p = 1.3 \cdot 10^{-22}$ *and* $F = 785.31$). In addition, a trend of difference increasing among densities can be observed as the specimens modified their spatial orientation from H-SO to V-SO.

The fracture toughness determined for modes I and II fracture were verified for statistically significance according to the PE and the SO (see Table 6). Without exception, significant differences among K_{IC} results and K_{IIC} results were determined ($p \ll 0.05$).

Therefore, the PE used for sinterization on one hand and the SO of the specimen in the building envelope on the other hand are directly and strongly influencing the fracture toughness. As orientation modifies from H-SO to V-SO, larger influence of the PE is recorded (exponential decrease of *p value*) for specimens subjected to mode I fracture. On the other hand, a reversed phenomenon was determined for mode II fracture.

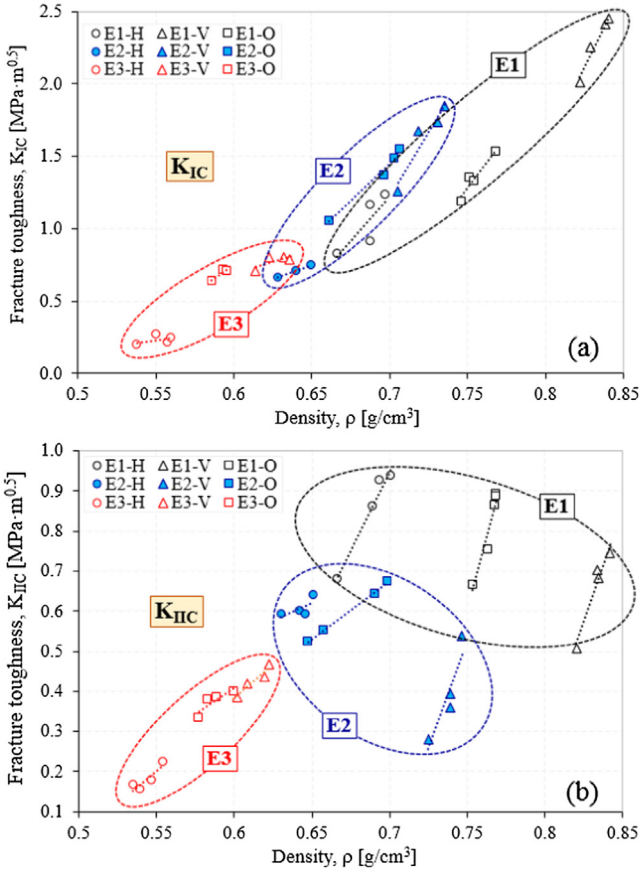

Fig. 12. Mode I (a) and mode II (b) fracture toughness variation with specimen density.

4. Conclusions

This paper presents the fracture toughness and geometrical properties of selectively sintered PA2200 polyamide in accordance to process energy (PE) and the spatial orientation (SO) of the specimens. Three PEs (E1, E2 and E3) and three SOs (O, V and H) have been considered as input variables and mode I and II fracture toughness (K_{IC} and K_{IIC}), density (ρ) and relative geometrical error of linear dimensions as output parameters.

The following conclusions can be drawn:

- Relative dimensional error of length (L), thickness (B) and width (W) are ranging from 0.32% to 9.12%, the larger error being recorded for thickness dimension in the lowest PE case (E3).
- The best dimensional stability was recorded for vertical direction (Z-axis of the machine), less dependent on PE.
- The best density was recorded for vertical orientation of the specimens, and as we expected for the highest PE.
- The higher mode I fracture toughness K_{IC} was recorded for vertical build (V) specimens, in the case of highest PE (E1). The K_{IC} ranges from 2.282 MPa·m$^{0.5}$ (E1 and V direction) to 0.232 MPa·m$^{0.5}$ (E3 and H direction).
- The higher K_{IIC} value was recorded for horizontal build (H) specimens, in the case of highest PE (E1). The K_{IIC} ranges from 0.836 MPa·m$^{0.5}$ (E1 and H direction) to 0.181 MPa·m$^{0.5}$ (E3 and H direction).
- Pearson's correlation reveals strong positive relationship of ρ with both input parameters (PE and SO) and also for K_{IC} while K_{IIC} has positive correlation only with PE and negative correlation with SO.
- One-way ANOVA analysis for ρ, K_{IC} and K_{IIC} parameters reveals statistically significant differences for every SO at each considered PE (P-val. $\ll$ 0.05).

CRediT authorship contribution statement

Emanoil Linul: Conceptualization, Investigation, Writing - original draft, Writing - review & editing. **Liviu Marsavina:** Resources, Conceptualization, Project administration, Validation, Supervision. **Dan Ioan Stoia:** Conceptualization, Methodology, Data curation, Writing-original draft, Writing - review & editing.

Declaration of Competing Interest

The authors declare that they have no known competing financial interests or personal relationships that could have appeared to influence the work reported in this paper.

Acknowledgement

The project leading to these results has received funding from the European Union's Horizon 2020 research and innovation program under grant agreement No 857124 *and* from Politehnica University of Timisoara, grant number GNaC2018 - ARUT, no. 1363/01.02.2019.

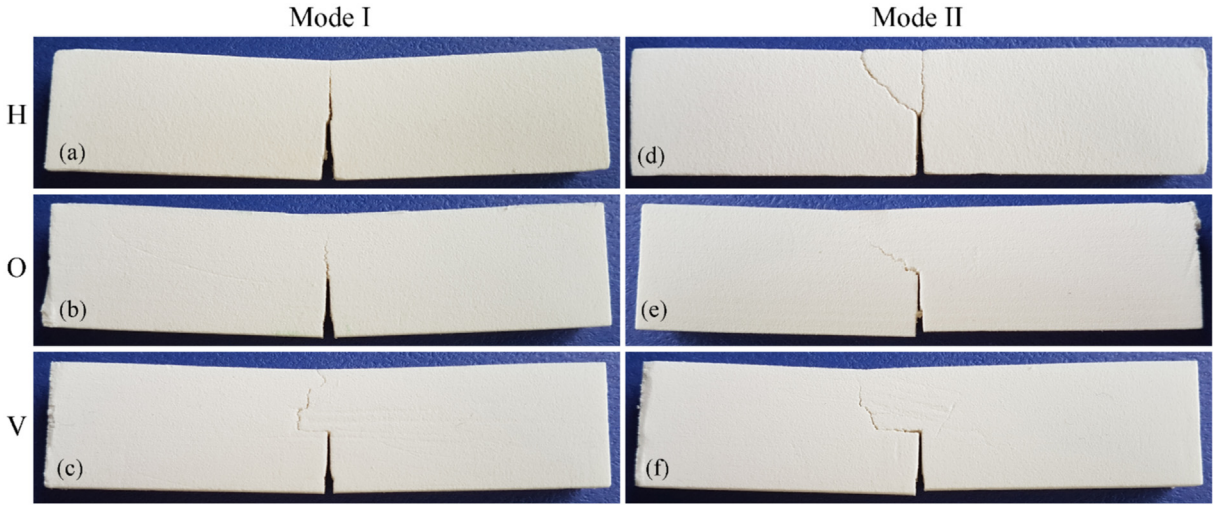

Fig. 13. Mode I (a-c) and mode II (d-f) crack propagation paths of Laser-Sintered Polyamide.

Table 4
Pearson's correlation of outcome parameters with energy and orientation.

Parameter	SO (E1)	Orient. (E2)	SO (E3)	PE (V)	PE (H)	PE (O)
ρ	0.9998	0.9744	0.9998	0.9147	0.9933	0.9428
L	−0.0820	0.9392	0.3621	0.9699	0.7948	0.7607
B	−0.8072	−0.8469	−0.9427	−0.7263	0.9120	−0.6013
W	0.9369	0.7864	0.7633	0.9493	−0.6549	−0.9158
K_{IC}	0.9510	0.9591	0.9912	0.9690	0.9477	0.6678
K_{IIC}	−0.9333	−0.7584	0.9575	0.9660	0.9481	0.9858

Table 5
ANOVA analysis of density.

SO	Source of Var.	SS	df	F	p	F crit.
H (0°)	BG	0.0836	2	95.0350	$1.1 \cdot 10^{-12}$	3.3690
	WG	0.0114	26			
O (45°)	BG	0.1187	2	254.9394	$2.0 \cdot 10^{-16}$	3.4221
	WG	0.0053	23			
V (90°)	BG	0.2056	2	785.3165	$1.3 \cdot 10^{-22}$	3.4028
	WG	0.0031	24			

Table 6
ANOVA analysis of fracture toughness for modes I and II fracture.

Mode	SO	Source of Var.	SS	df	F	p	F crit.
I (K_I)	H (0°)	BG	1.4296	2	11.3392	$1.7 \cdot 10^{-3}$	3.8852
		WG	0.7564	12			
	O (45°)	BG	1.8792	2	43.8015	$2.0 \cdot 10^{-5}$	4.2564
		WG	0.1930	9			
	V (90°)	BG	4.7695	2	153.3067	$1.0 \cdot 10^{-7}$	4.2564
		WG	0.1400	9			
II (K_{II})	H (0°)	BG	0.9547	2	65.2197	$7.9 \cdot 10^{-7}$	3.9822
		WG	0.0805	11			
	O (45°)	BG	0.4280	2	41.5741	$7.4 \cdot 10^{-6}$	3.9822
		WG	0.0566	11			
	V (90°)	BG	0.2053	2	7.7639	$6.8 \cdot 10^{-3}$	3.8852
		WG	0.1586	12			

Appendix A. Supplementary material

Supplementary data to this article can be found online at https://doi.org/10.1016/j.tafmec.2020.102497.

References

[1] D.T. Pham, R.S. Gault, A comparison of rapid prototyping technologies, Int. J. Mach. Tool. Manu. 38 (1998) 1257–1287.
[2] G.V. Salmoria, C.H. Ahrens, P. Klauss, et al., Rapid manufacturing of polyethylene parts with controlled pore size gradients using Selective Laser Sintering, Mater. Res. 10 (2007) 211–214.
[3] W.Y. Yeong, C.K. Chua, Implementing additive manufacturing for medical devices: a quality perspective, Proc. of the 6th Int. Conf. on Adv. Res. in Virtual and Rapid Prototyping, Leiria-Portugal, 1–5 Oct. 2013, 2013, pp. 115–120.
[4] S. Griessbach, R. Lach, W. Grellmann, Structure–property correlations of laser sintered nylon 12 for dynamic dye testing of plastic parts, Polym. Test. 29 (2010) 1026–1030.
[5] O.S. Es-Said, J. Foyos, R. Noorani, et al., Effect of layer orientation on mechanical properties of rapid prototyped samples, Mater. Manuf. Process. 15 (2000) 107–122.
[6] A.A. Mousa, Experimental investigations of curling phenomenon in selective laser sintering process, Rapid Prototyp. J. 22 (2006) 405–415.
[7] M. Crespo, M.T. Gómez-del Río, J. Rodríguez, Failure of SLS polyamide 12 notched samples at high loading rates, Theor. Appl. Fract. Mech. 92 (2017) 233–239.
[8] ASTM 638-03, Standard test method for tensile properties of plastics, 2003.
[9] J. Zhang, A. Fatemi, Surface roughness effect on multiaxial fatigue behavior of additive manufactured metals and its modeling, Theor. Appl. Fract. Mech. 103 (2019) 1–11.
[10] R. Ghandriz, K. Hart, J. Li, Extended finite element method (XFEM) modeling of fracture in additively manufactured polymers, Addit. Manuf. 31 (2020) 1–9.
[11] D.I. Stoia, L. Marşavina, E. Linul, Correlations between process parameters and outcome properties of Laser-Sintered Polyamide, Polymers 11 (2019) 1850.
[12] A. Pilipović, T. Brajlih, I. Drstvenšek, Influence of processing parameters on tensile properties of SLS polymer product, Polymers 10 (2018) 1208.
[13] D.I. Stoia, E. Linul, L. Marsavina, Influence of manufacturing parameters on mechanical properties of porous materials by Selective Laser Sintering, Materials 12 (2019) 871.
[14] G. Craft, J. Nussbaum, N. Crane, J.P. Harmon, Impact of extended sintering times on mechanical properties in PA-12 parts produced by powder bed fusion processes, Addit. Manuf. 22 (2018) 800–806.
[15] P. Poapongsakorn, L.A. Carlsson, Fracture toughness of closed-cell PVC foam: Effects of loading configuration and cell size, Compos. Struct. 102 (2013) 1–8.
[16] A. Riemer, H.A. Richard, J.P. Brüggemann, J.N. Wesendahl, Fatigue crack growth in additive manufactured products, Frattura ed Integrità Strutturale. 34 (2015) 437–446.
[17] L. Marsavina, D.M. Constantinescu, E. Linul, et al., Experimental and numerical crack paths in PUR foams, Eng. Fract. Mech. 167 (2016) 68–83.
[18] E. Linul, D.A. Serban, L. Marsavina, Influence of cell topology on mode I fracture toughness of cellular structures, Phys. Mesomech. 21 (2) (2018) 178–186.
[19] J.P. Reis, M.F.S.F. de Moura, R.D.F. Moreira, F.G.A. Silva, Pure mode I and II interlaminar fracture characterization of carbon-fibre reinforced polyamide composite, Compos. Part B-Eng. 169 (2019) 126–132.
[20] M.R.M. Aliha, S.S. Mousavi, A. Bahmani, et al., Crack initiation angles and propagation paths in polyurethane foams under mixed modes I/II and I/III loading, Theor. Appl. Fract. Mech. 101 (2019) 152–161.
[21] E. Moradi, A. Zeinedini, On the mixed mode I/II/III inter-laminar fracture toughness of cotton/epoxy laminated composites, Theor. Appl. Fract. Mech. 105 (2020) 1–10.
[22] Z. Daneshjoo, L. Amaral, R.C. Alderliesten, et al., Development of a physics-based theory for mixed mode I/II delamination onset in orthotropic laminates, Theor. Appl. Fract. Mech. 103 (2019) 102303.
[23] E. Linul, L. Marşavina, C. Vălean, R. Bănică, Static and dynamic mode I fracture toughness of rigid PUR foams under room and cryogenic temperatures, Eng. Fract. Mech. 225 (2020) 106274.
[24] E. Linul, L. Marsavina, Prediction of fracture toughness for open cell polyurethane foams by finite element micromechanical analysis, Iran. Polym. J. 20 (9) (2011) 736–746.
[25] M.R.M. Aliha, S.S. Mousavi, S.M.N. Ghoreishi, Fracture load prediction under mixed mode I + II using a stress based method for brittle materials tested with the asymmetric four-point bend specimen, Theor. Appl. Fract. Mech. 103 (2019) 102249.
[26] Y. Yin, Y. Qiao, S. Hu, Four-point bending tests for the fracture properties of concrete, Eng. Fract. Mech. 211 (2019) 371–381.
[27] M.F.S.F. de Moura, M.A.L. Silva, J.J.L. Morais, N. Dourado, Mode II fracture characterization of wood using the Four-Point End-Notched Flexure (4ENF) test, Theor. Appl. Fract. Mech. 98 (2018) 23–29.
[28] M. Heidari-Rarani, M.R.M. Aliha, M.M. Shokrieh, M.R. Ayatollahi, Mechanical durability of an optimized polymer concrete under various thermal cyclic loadings-An experimental study, Constr. Build. Mater. 64 (2014) 308–315.
[29] M. Fakhri, E. Amoosoltani, M.R.M. Aliha, Crack behavior analysis of roller compacted concrete mixtures containing reclaimed asphalt pavement and crumb rubber, Eng. Fract. Mech. 180 (2017) 43–59.
[30] H. Rooholamini, A. Hassani, M.R.M. Aliha, Evaluating the effect of macro-synthetic fibre on the mechanical properties of roller-compacted concrete pavement using response surface methodology, Constr. Build. Mater. 159 (2018) 517–529.
[31] H. Rooholamini, A. Hassani, M.R.M. Aliha, Fracture properties of hybrid fibre-reinforced roller-compacted concrete in mode I with consideration of possible kinked crack, Constr. Build. Mater. 187 (2018) 248–256.
[32] S.M.J. Razavi, M.R.M. Aliha, F. Berto, Application of an average strain energy density criterion to obtain the mixed mode fracture load of granite rock tested with the cracked asymmetric four-point bend specimens, Theor. Appl. Fract. Mech. 97 (2017) 419–425.
[33] C. Wang, Z.M. Zhu, H.J. Liu, On the I-II mixed mode fracture of granite using four-point bend specimen, Fatigue Fract. Eng. Mater. Struct. 39 (10) (2016) 1193–1203.
[34] M.R.M. Aliha, M.R. Ayatollahi, B. Kharazi, Numerical and experimental investigations of mixed mode fracture in granite using four-point-bend specimen, Damage and Fracture Mechanics, Springer, Dordrecht, 2009, pp. 275–283.
[35] D.A. Apostol, F. Stuparu, D.M. Constantinescu, et al., Crack length influence on stress intensity factors for the asymmetric four-point bending testing of a polyurethane foam, Mater. Plast. 53 (2) (2016) 280–282.
[36] X.T. Miao, Q. Yu, C.Y. Zhou, et al., Experimental and numerical investigation on fracture behavior of I-II mixed mode crack for commercially pure Titanium, Theor. Appl. Fract. Mech. 96 (2018) 202–215.
[37] H. Yoshihara, M. Maruta, Mode I J-integral of extruded polystyrene measured by the four-point single-edge notched bending test, Eng. Fract. Mech. 222 (2019) 106716.
[38] M.M. Mirsayar, A. Razmi, M.R.M. Aliha, F. Berto, EMTSN criterion for evaluating

mixed mode I/II crack propagation in rock materials, Eng. Fract. Mech. 190 (2018) 186–197.
[39] M.M. Mirsayar, F. Berto, M.R.M. Aliha, P. Park, Strain-based criteria for mixed-mode fracture of polycrystalline graphite, Eng. Fract. Mech. 156 (2016) 114–123.
[40] A.R. Torabi, M.H. Kalantari, M.R.M. Aliha, S.M.N. Ghoreishi, Pure mode II fracture analysis of dissimilar Al-Al and Al-Cu friction stir welded joints using the generalized MTS criterion, Theor. Appl. Fract. Mech. 104 (2019) 102369.
[41] H.R. Fattahi Amirdehi, M.R.M. Aliha, A. Moniri, A.R. Torabi, Using the generalized maximum tangential stress criterion to predict mode II fracture of hot mix asphalt in terms of mode I results-a statistical analysis, Constr. Build. Mater. 213 (2019) 483–491.
[42] M.R.M. Aliha, F. Berto, A. Bahmani, P. Gallo, Mixed mode I/II fracture investigation of Perspex based on the averaged strain energy density criterion, Phys. Mesomech. 20 (2) (2017) 149–156.
[43] S.S. Mousavi, M.R.M. Aliha, D.M. Imani, On the use of edge cracked short bend beam specimen for PMMA fracture toughness testing under mixed-mode I/II, Polym. Test. 81 (2020) 106199.
[44] A.A. Ahmed, L. Susmel, A material length scale–based methodology to assess static strength of notched additively manufactured polylactide (PLA), Fatig. Fract. Eng. Mater. Struct. 41 (2018) 2071–2098.
[45] S.M.J. Razavi, F. Berto, Fatigue strength of notched specimens made of Ti-6Al-4V produced by Selected Laser Melting technique, Proc. Struct. Integr. 13 (2019) 74–78.
[46] K. Solberg, J. Torgersen, F. Berto, Fatigue behaviour of additively manufactured inconel 718 produced by Selective Laser Melting, Proc. Struct. Integr. 13 (2018) 1762–1767.
[47] ISO 13320, Particle size analysis- Laser diffraction methods, International Organization for Standardization; 1214 Vernier, Geneva, Switzerland, 2009, pp. 51.
[48] ISO 60, Plastics - Determination of apparent density of material that can be poured from a specified funnel, International Organization for Standardization; 1214 Vernier, Geneva, Switzerland, 1977, pp. 2.
[49] ISO 11357-1, Plastics - Differential scanning calorimetry (DSC) - Part 1: General principles, International Organization for Standardization; 1214 Vernier, Geneva, Switzerland, 2016, pp. 33.
[50] ISO 10993-1, Biological evaluation of medical devices - Part 1: Evaluation and testing within a risk management process; International Organization for Standardization; 1214 Vernier, Geneva, Switzerland, 2018, pp. 41.
[51] EOS GmbH Product information, Available online: www.eos.info/material-p (accessed on 09 November 2018).
[52] ASTM D5045, Standard test methods for plane-strain fracture toughness and strain energy release rate of plastic materials, 1999.
[53] D.A. Apostol, F. Stuparu, D.M. Constantinescu, et al., Experimental and XFEM analysis of Mode II propagating crack in a polyurethane foam, Mater. Plast. 53 (4) (2016) 685–688.
[54] M.R. Ayatollahi, M.R.M. Aliha, On the use of an anti-symmetric four-point bend specimen for mode II fracture experiments, Fatig. Fract. Eng. Mater. Struct. 34 (11) (2011) 898–907.
[55] M.R.M. Aliha, M.R. Ayatollahi, B. Kharazi, Mode II brittle fracture assessment using ASFPB specimen, Int. J. Fract. 159 (2) (2009) 241–246.
[56] D.K. Rajak, N.N. Mahajan, E. Linul, Crashworthiness performance and micro-structural characteristics of foam-filled thin-walled tubes under diverse strain rate, J. Alloy. Compd. 775 (2019) 675–689.
[57] M.R.M. Aliha, E. Linul, A. Bahmani, L. Marsavina, Experimental and theoretical fracture toughness investigation of PUR foams under mixed mode I+III loading, Polym. Test. 67 (2018) 75–83.
[58] S. Pirmohammad, M. Hojjati Mengharpey, A new mixed mode I/II fracture test specimen: Numerical and experimental studies, Theor. Appl. Fract. Mech. 97 (2018) 204–214.
[59] E. Linul, L. Marşavina, P.A. Linul, J. Kovacik, Cryogenic and high temperature compressive properties of Metal Foam Matrix Composites, Compos. Struct. 209 (2019) 490–498.
[60] N. Movahedi, E. Linul, L. Marsavina, The temperature effect on the compressive behavior of closed-cell aluminum-alloy foams, J. Mater. Eng. Perform. 27 (1) (2018) 99–108.
[61] L. Marsavina, F. Berto, R. Negru, et al., An engineering approach to predict mixed mode fracture of PUR foams based on ASED and micromechanical modeling, Theor. Appl. Fract. Mech. 91 (2017) 148–154.
[62] T. Voiconi, E. Linul, L. Marsavina, T. Sadowski, M. Knec, Determination of flexural properties of rigid PUR foams using digital image correlation, Solid State Phenom. 216 (2014) 116–121.
[63] Y. Murakami, Stress Intensity Factors Handbook, Pergamon Press, New York, 1987.
[64] M.Y. He, J.W. Hutchinson, Asymmetric four-point crack specimen, J. Appl. Mech. 67 (2000) 207–209.
[65] D. Scorza, L. Marsavina, A. Carpinteri, et al., Size-effect independence of particle-board fracture toughness, Compos. Struct. 229 (2019) 111374.
[66] L. Marsavina, D.M. Constantinescu, E. Linul, T. Voiconi, D.A. Apostol, Shear and mode II fracture of PUR foams, Eng. Fail. Anal. 58 (2015) 465–476.
[67] E. García Plaza, P.J.N. López, M.Á.C. Torija, J.M.C. Muñoz, Analysis of PLA geometric properties processed by FFF additive manufacturing: Effects of process parameters and plate-extruder precision motion, Polymers 11 (2019) 1581.